



Strain mapping at the micro-scale in hierarchical polymer composites with aligned carbon nanotube grafted fibers



Mahoor Mehdikhani ^{a, *}, Anna Matveeva ^{a, b}, M. Ali Aravand ^{a, c, d}, Brian L. Wardle ^c,
Stepan V. Lomov ^a, Larissa Gorbatikh ^{a, b}

^a KU Leuven, Department of Materials Engineering, Kasteelpark Arenberg 44, 3001, Leuven, Belgium

^b Center for Design, Manufacturing and Materials, Skolkovo Institute of Science and Technology, Nobel St. 3, Skolkovo Innovation Center, Moscow, 143026, Russia

^c Department of Aeronautics and Astronautics, Massachusetts Institute of Technology, 77 Massachusetts Ave, Cambridge, MA, 02139, USA

^d Queen's University Belfast, School of Mechanical and Aerospace Engineering, Belfast, BT9 5AH, UK

ARTICLE INFO

Article history:

Received 7 June 2016

Received in revised form

17 October 2016

Accepted 23 October 2016

Available online 24 October 2016

Keywords:

Digital image correlation (DIC)

Scanning electron microscopy (SEM)

Carbon nanotubes

Mechanical properties

Finite element analysis (FEA)

ABSTRACT

For the first time, micro-scale digital image correlation (μ DIC) is investigated for measurement of strain fields in hierarchical fiber-reinforced composites. The methodology is developed on an exemplary alumina fiber/epoxy composite laminate with aligned carbon nanotubes (A-CNTs) grown on fibers. Utilizing environmental scanning electron microscopy and nano-scale random speckle patterns, sufficient precision is achieved to detect the influence of the A-CNTs on the deformation field around the fibers. Debonded regions at the fiber/matrix interface with openings as small as 35 nm could be detected. μ DIC could identify the propagation of the debonded region based on the non-linear increase of the opening. The image correlation uncertainty in the displacement analysis is estimated to be below 5 nm. The experimental results are validated by computational analysis performed on the region of interest. For this, an advanced model with two scales of reinforcement (microscopic fibers and nanotubes) and boundary conditions taken from the experiment is used. As verified by the model, A-CNTs are found to constrain matrix deformation in their longitudinal direction.

© 2016 Elsevier Ltd. All rights reserved.

1. Introduction

Digital image correlation (DIC) is a popular technique to measure deformation on the surface of a material during loading [1,2]. Theoretically, DIC can be applied at any scale provided images for analysis are available at that scale. At the macro- and meso-scale, DIC is now widely used to study deformation of different materials including fiber-reinforced composites [3–6]. When it comes to the analysis of micro-scale heterogeneity, DIC has to be combined with microscopy and it is known as micro-scale DIC (μ DIC) [7–10]. In μ DIC, one is confronted with many challenges including application of a small-scale random speckle pattern, imaging distortions and noise as well as stress relaxation during image acquisition in case of long capture time [9–11]. Due to these challenges, studies of fiber-reinforced composites employing μ DIC are scarce. This is despite an increasing interest in realization of the microscopic

phenomena taking place in these materials. The potential of μ DIC to analyze deformations in composite materials at the micro-scale was assessed in Refs. [12,13]. High-resolution and low-error micro-scale strain maps could be obtained, thus further supporting the use of this technique in composites.

The next-generation structural materials are envisioned to be hierarchically designed down to the nano-scale. Carbon nanomaterials like carbon nanotubes (CNTs) and graphene show promise in the development of structural composites with superior toughness and added functionality [14–17]. Their effect on deformation and damage development at the micro-scale has not yet been well understood. Reliable techniques such as μ DIC are needed to promote investigations in this direction.

In the present study, we explore the applicability of μ DIC to the nano-engineered composites using our previously developed methodology on conventional composites [13]. The study is performed on an alumina fiber/epoxy composite with CNT grafted fibers (also known as “fuzzy” fibers) that is loaded under transverse 3-point bending inside an Environmental Scanning Electron Microscope (ESEM). The focus is on micro-scale features resulting

* Corresponding author.

E-mail address: mahoor.mehdikhani@kuleuven.be (M. Mehdikhani).

from the presence of fibers and CNTs, and on micro-scale phenomena like debonding at the fiber/matrix interface. A high-quality random speckle pattern, optimum correlation parameters, and proper microscopy settings, which are required for an accurate identification of the micro-features and micro-phenomena with μ DIC, are provided.

We also validate the experimentally measured deformations against numerical predictions. The validation for composites is typically done using modeling approaches, for example, Finite Element Analysis (FEA), which provides high-accuracy solutions and can be used at different scales. In the case of nano-engineered fiber-reinforced composites, the application of Finite Element (FE) modeling is rather challenging. This is due to the scale difference between nanotubes and fibers as well as geometrical complexity of CNT assemblies. Three-dimensional (3D) computational models of fiber-reinforced composites with CNTs are rare and approaches differ. In Refs. [18,19], a multiple-step modeling strategy was proposed to include reinforcements of two scales, where CNTs were modeled as straight cylinders. In Refs. [20–22], fibers and CNTs were modeled simultaneously and a large variety of CNT configurations could be reproduced, including CNTs deposited on fibers with different alignment and orientation. In the current work, we use the latter method to derive displacement and strain fields as reference solutions to check the accuracy of μ DIC measurements.

2. Materials

The micro-scale reinforcements are continuous alumina fibers, woven into a plain weave (*Cotronics Ultra-Temp 391*) with an areal density of 371 g/m². For catalyst deposition, the fabric was soaked in a 50 mM solution of iron nitrate ($\text{Fe}(\text{NO}_3)_3 \cdot 9\text{H}_2\text{O}$, *Alfa Aesar*) in isopropanol, and dried overnight at -30°C . Swatches were cut from the catalyst-deposited fabric and placed in a tube furnace. The catalyst coating was reduced to Fe particles under the hydrogen

flow at 650°C . Then, ethylene was introduced at the same temperature to start the CNT growth. After ~ 3 min of ethylene exposure, long and radially Aligned CNTs (A-CNTs) were grown on the surface of the fibers. The A-CNT growth exhibits a “Mohawk” morphology [23] and the length of the nanotubes is ~ 17 – $19\ \mu\text{m}$ (Fig. 1). The stack of five plies was dried under vacuum at 150°C for 2 h before it was infused with the *RTM-6* resin (*Hexcel*) by the Vacuum Assisted Resin Infusion (VARI) method. The resin was degassed under vacuum at 80°C before the infusion. The infusion was done at 90°C , and the laminate was then cured at 160°C for 4 h and post-cured at 180°C for another 4 h. The hierarchy of this composite material is illustrated in Fig. 2. The internal structure of this material was studied in Ref. [24] (referred there as “Long”).

3. μ DIC methodology

The μ DIC methodology consists of specimen preparation, speckle patterning, pattern evaluation, mechanical loading, image acquisition, microscopy assessment, optimizing DIC parameters, applying DIC, error analysis, and FEA validation. It is similar to the one applied to conventional composites in Ref. [13].

3.1. Specimen preparation, speckle patterning, pattern evaluation

A $58.3 \times 8.2 \times 3.1\text{-mm}^3$ specimen is cut from the composite laminate described in Section 2. One of the two cross-sections is grinded and polished. The speckle patterning method is as follows. A 0.05 wt% water-based suspension of alumina particles with the average size of 220 nm (*TM-DAR* series of *TAIMICRON*), containing 0.005 wt% *DARVAN-CN* for stabilization of the suspension, is prepared using ultrasonication and magnetic stirring. The suspension is applied to the polished surface of the specimen. After being dried in the ambient air, the deposition is repeated. This way, proper dispersion and distribution of particles are expected. The speckled

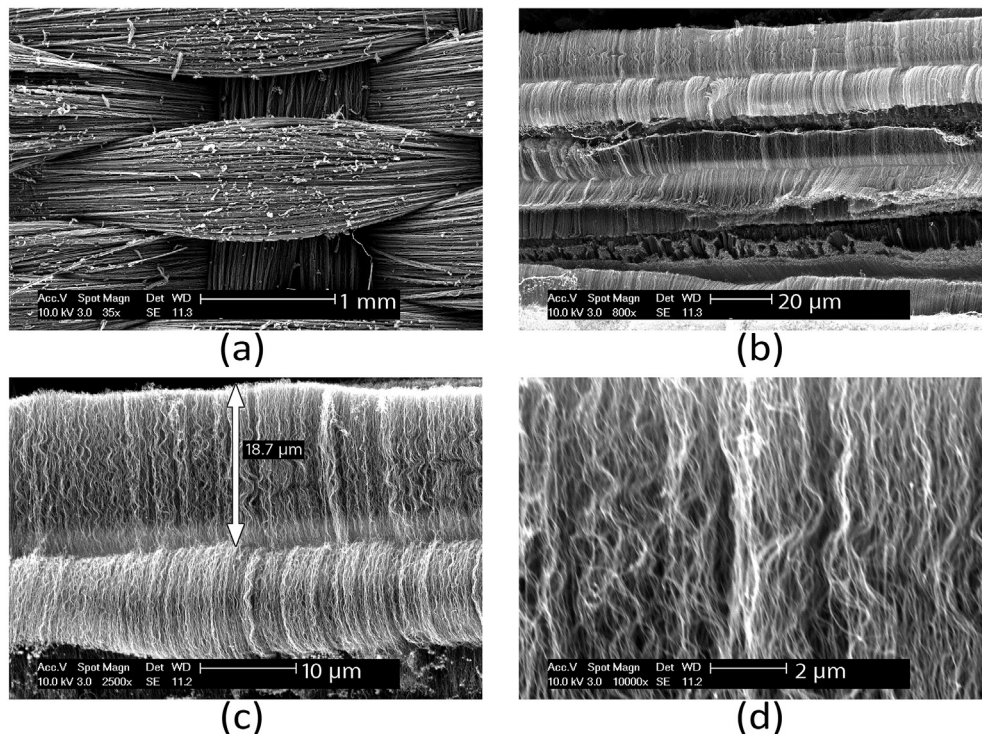


Fig. 1. Micrographs of the A-CNT grown on the alumina fabric with a zoom-in on (a) textile (woven) structure (35 \times), (b) fibers inside yarns (800 \times), (c) single fiber (2500 \times), and (d) nanotubes inside the forest (10000 \times) - (a) and (c) are also presented in Ref. [24].

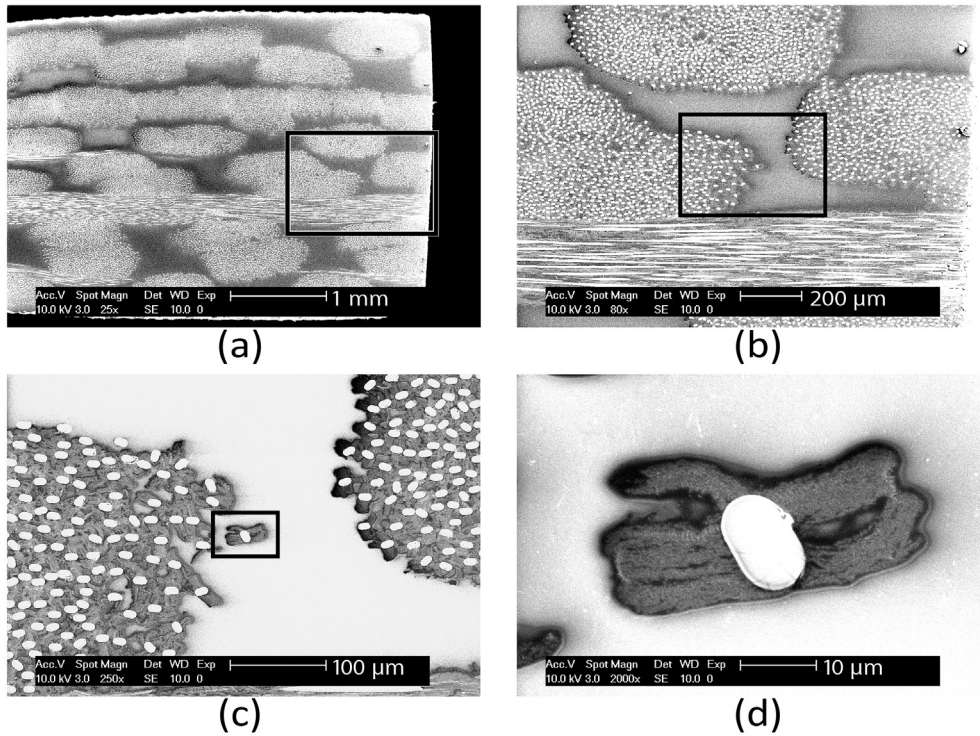


Fig. 2. Hierarchy of the “Long” A-CNT-grafted alumina fiber/epoxy composite in micrographs from (a) textile (woven) laminate (25×), (b) yarn cross-sections (80×), (c) fibers inside yarns (250×), and (d) A-CNT forests on a single fiber (2000×) – rectangles show the field of view for the subsequent micrograph.

surface is coated with a thin film of gold, applied through an optimized sputtering process.

After speckling, the quality of the speckle pattern is appraised through so-called “strain deviation analysis” [13]. For this, a 1424×968 -pixel² micrograph (Fig. 3b) with the area of $103 \times 70 \mu\text{m}^2$ of the speckled surface is acquired through electron microscopy with the imaging parameters mentioned in Section 3.2. The micrograph is digitally elongated by 12 pixels, using *lanczos3* method in *MATLAB*. This is equivalent to a virtual deformation of 0.008462 for the horizontal component of the Lagrangian strain. DIC is applied to the entire digitally deformed image with subset,

step, and filter sizes of 21 and 5 pixels, and 15 data points, respectively. The correlation is done with *VIC-2D 2009* software (*Correlated Solutions*). *Normalized squared differences* criterion, *optimized 4-tap* interpolation, and *Gaussian* subset weights are employed for correlation (also for further correlations). The resulting average horizontal strain as obtained by DIC is 0.008474, and after reduction of interpolation heterogeneity resulting from digital resizing [13], the standard deviation is 0.000067. Hence, the coefficient of variation, which is the relative standard deviation, is 0.79%. Since the obtained average strain is close to the (virtually) applied strain of 0.008462, and the relative standard deviation

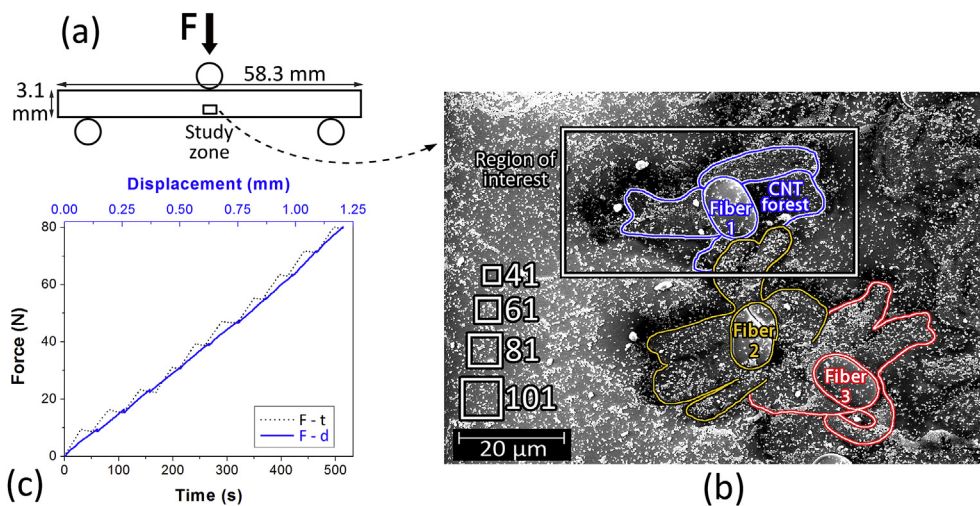


Fig. 3. The “study zone” chosen for strain mapping, shown (a) schematically on the specimen in 3-point bending and (b) at the working magnification (1200×) with colored edges of A-CNT forests grown on the three alumina fibers – the examined subsets are shown on the micrograph representing their actual size – the window around *Fiber 1* displays the selected “region of interest” for FE modeling; (c) stepwise macro load versus displacement and time.

(exhibiting the measurement error) is low, it is concluded that the produced random speckle pattern is adequate for strain measurement at this scale. This speckle application approach was optimized in Ref. [13] for composites without nano-modifications.

3.2. Mechanical loading, image acquisition, microscopy assessment

The speckled specimen is mounted in a mini-tester stage (*Deben UK Limited*), installed inside an ESEM chamber (*FEI/Philips XL30 ESEM FEG*) for 3-point bending. Carbon tape is used to establish conductivity between specimen surface and the stage for diminishing the charging effect. A suitable “study zone” including three semi-isolated alumina fibers (referred to as *Fiber 1*, *Fiber 2*, and *Fiber 3*) with well-aligned CNT forests on them is identified in the tensile (bottom) edge of the specimen, close to the middle line (Fig. 3a and b). Prior to loading, four micrographs are captured from the study zone in 1-min intervals. Since the sample did not experience any motion and deformation in these micrographs, they are referred to as *still-rigid-body* micrographs. Transverse 3-point bending is then applied to the specimen with a speed of 0.2 mm/min, and force is measured using a 200-N load cell. Every 30 s, the loading is stopped, the study zone is located, and a micrograph is captured. The maximum total time for finding and scanning the study zone is 30 s. The stepwise loading is continued until the global bending force reaches 79.9 N, corresponding to a 1.2-mm maximum deflection (Fig. 3c). In total, 11 micrographs, with the resolution of $1424 \times 968 \text{ pixel}^2$ ($103 \times 70 \mu\text{m}^2$) are acquired from the consecutive loading steps. The micrographs are taken at $1200\times$ magnification using Secondary Electron (SE) detector, high definition filter, 10.0 kV voltage, 5.0 spot size, 6.7 ms linetime, and 968 line/frame.

DIC is applied to the four still-rigid-body micrographs to investigate the microscopy quality. The subset, step, and filter sizes are 61 pixels, 2 pixels, and 15 data points, respectively. The values are selected based on the parameter optimization, explained in Section 3.3. Although ideally, the resulting strain should be zero for the still-rigid-body DIC, the analysis reveals that for the horizontal component, the resulting mean strain for each micrograph is between 0.000177 and 0.000299, and the standard deviation is between 0.000524 and 0.000626. These spurious strains are caused chiefly by microscopy imperfections, as explained in Section 3.3. The highest local (absolute) value of these strains, which are in general higher on fibers, is 0.001820. The greater values of the spurious strains on fibers may be explained by higher charging of fibers and their lower coverage by speckles. The latter can be attributed to the difference in surface energy of the fibers versus the matrix, and/or differences in surface height of fibers and matrix after polishing. The deformation of fibers themselves is of less interest in this study, compared to that of the matrix and CNT forests.

3.3. DIC parameter optimization, applying DIC, error analysis

Subset, step, and filter sizes have a significant influence on the accuracy of DIC measurements. Hence, the strain deviation analysis was performed to select optimum values for these parameters. The virtual deformation in Section 3.1, which is equivalent to 0.008462 of horizontal strain, is analyzed with different sets of DIC parameters. Based on the analysis in Ref. [13], the examined subset sizes are 41, 61, 81, and 101 pixels (shown on Fig. 3b), step sizes are 1, 2, 5, and 7 pixels, and filter sizes are 5, 15, and 25 data points. The resulting average of horizontal strain for each set of parameters is between 0.008465 and 0.008483, which shows an error below 0.25% relative to the applied virtual strain, i.e. 0.008462. The relative standard deviation of the strain deviation field, after diminution of resizing interpolation heterogeneity, is between 0.28 and 1.38%, showing a small measurement error. It is observed that

increase in the size of the parameters decreases the standard deviation, which means reduction in measurement error. At the same time, a general consequence of the increase in the parameter sizes is reduction in the analysis resolution [1]. Therefore, a trade-off should be considered in choosing appropriate DIC parameters. Considering this trade-off and based on the results of the strain deviation analysis, the selected values for subset, step, and filter sizes are 61 pixels ($4.42 \mu\text{m}$), 2 pixels ($0.14 \mu\text{m}$), and 15 data points ($2.17 \mu\text{m}$), respectively. DIC with the optimized parameters is then applied to the 11 micrographs of the study zone, taken during deformation.

If micrographs of a deforming specimen are obtained with an (E) SEM, the stress relaxation during image acquisition as well as imperfections of SEM imaging, which are mainly drift and spatial distortions and random noise, can disturb the μDIC measurements. The time-dependent drift distortion can be due to motion of the microscope stage, heating of the electron column components or the sample itself. Charging of contaminants on deflectors and apertures, charging of the microscope stage or sample, and disturbance from magnetic fields may further contribute to this distortion. The spatial distortion is similar to the lens distortion in optical microscopy, and can vary from test to test. Finally, the random noise, which disturbs electron microscopy much more than optical microscopy, has a strong dependency on imaging parameters. Therefore, by choosing appropriate parameters, it is possible to substantially reduce the noise. These imaging issues, appearing as potential error sources for μDIC , are extensively explored in Refs. [9–11], where methods to deal with them are presented. According to Ref. [2], results of 2D DIC can be disturbed by two types of errors: physical and correlation-based. Physical errors have sources such as poor speckle pattern, imaging (distortions and noise), out-of-plane displacement, and stress-relaxation [2,9–11]. The combination of poor speckle pattern, imaging, and correlation-based errors can be estimated through still-rigid-body DIC. Since the imaging errors are much higher than the other two in the present study, this combination is referred to as *microscopy error*. The still-rigid-body analysis was performed in Section 3.2, revealing that the maximum values for mean strain, standard deviation, and local strain resulting from microscopy error are 0.000299, 0.000626, and 0.001820, respectively. On the other hand, the parameter optimization analysis above estimates the speckle pattern and correlation-based errors, of which the combination is referred to as *measurement error* in the present study. In the strain deviation analysis with the optimum parameters, the difference between the calculated mean strain and the applied strain is 0.000014, the resulting standard deviation is 0.000091, and the maximum local strain deviation from the applied strain is 0.000600, corresponding to the measurement error. The low values for microscopy and measurement errors, resulting from high-quality speckle pattern, optimum DIC parameters, and proper microscopy settings, ensure an adequate quality for μDIC analysis in the present study. No imaging correction methods, such as those proposed in Refs. [9–11], are employed.

4. Computational model for validation

4.1. Geometry

The μDIC measurements are validated against predictions of FEA. To decrease heavy computational costs, a smaller “region of interest” ($55.5 \times 27.6 \mu\text{m}^2$), containing a single alumina fiber (*Fiber 1*) with grafted strands of A-CNTs (Fig. 3b), is selected. The cross-section of the alumina fiber has a “racetrack” shape. The length of the rectangular part, radii of caps, and position/inclination of the cross-section were taken from the micrograph of the region of

interest (Fig. 3b). The 3D curved geometries of center lines of A-CNTs were determined from the higher-magnification micrographs of the dry A-CNT-grafted fibers (Fig. 1c and d). Nanotubes, which were clearly distinguished on the image, had a quasi-helical curved geometric shape with multiple perversions. *ImageJ* software was employed to measure the pitches and radii of the observed helices. The pitch and radius frequency distributions were used to model nanotubes, each as a sequence of helical sections with different pitches and radii. To ensure continuity between two consecutive helical sections, the radius within one section had a linear growth toward the radius assigned for the next section. The handedness of the helices was chosen randomly. To generate the nanotubes, the starting vertices were uniformly distributed over the fiber surface using *von Neumann* acceptance-rejection sampling. The number of helical sections was defined by the length of the nanotube, which was kept below 18 μm for the forest grown on *Fiber 1*, and below 15 μm for the forest grown on *Fiber 2*, but cropped to the size of the region of interest. The generated FE model is displayed in Fig. 4a.

The orientation of nanotubes was captured from the micrograph (Fig. 3b). The A-CNT forest was divided into several parts, each was highlighted in *ImageJ* and presented as a polygon, of which the boundaries were used as spatial constraints during the CNT generation. In each polygon, nanotubes had a preferred orientation, which could be changed in order for nanotubes to stay inside the polygon. The amount of nanotubes in the corresponding parts depends on the area of the part and the volume fraction of nanotubes in the forest, which is considered equal to 2.8% in the present study. The latter was calculated from the mass ratio between the fiber and CNT, known from the growth process. A depth of 0.5 μm , in the fiber (z) direction, is assigned for the 3D model of the region of interest, which results in a computationally manageable model. In the fiber (z) direction, periodic boundary conditions were applied to guarantee continuity of those CNTs that went out of the boundaries. Cylindrical hollow CNTs were then obtained by performing a shell sweep of a circle with radius of 9 nm [25] along the constructed curves (Fig. 4c). The thickness of the CNT cylinder wall was set to 3.5 nm corresponding approximately to 10 layers of graphene [26].

According to the micrograph (Fig. 3b), the matrix/fiber interface was partly debonded at two places. The extent of the debonded region was estimated, and introduced to the model: 36% of the *Fiber 1* surface, on the right side of the fiber, and 20% on the left side were initially debonded from the matrix. The debonded regions were modeled as traction-free surfaces between the fiber and the matrix, along the entire fiber length in the z direction. The size of the debonded regions was fixed during simulation. The remaining

interface was assumed to be perfectly bonded, namely the fiber and the matrix shared the same nodes.

4.2. Material properties

Epoxy and alumina fiber were modeled as isotropic solids with a Young's modulus of 3.0 GPa and a Poisson's ratio of 0.4 for epoxy, and a Young's modulus of 134 GPa [27], a Poisson's ratio of 0.25, and a density of 3.9 g/cm^3 [28] for the fiber. The CNTs were modeled as shells with isotropic properties with a Young's modulus of 500 GPa [29], a Poisson's ratio of 0.3 and a density of 2.0 g/cm^3 [30]. Linear elastic behavior was assumed for all three phases.

4.3. Mesh and boundary conditions

To keep numerical efforts and mesh generation in the FEA at the manageable level, the embedded element technique was used. In this technique, shell elements representing the nanotubes are overlaid on the solid elements representing the polymer matrix. Similar superposition models have been used in a number of works on composite modeling [20,22,31,32]. Special attention was paid to the meshing procedure. Previously, it was shown that the accuracy of the results strongly depends on the mesh quality, namely the appropriate size and type of elements [33–35]. Here, the matrix is discretized by free meshes using 8-node brick elements with one integration point and linear shape functions. The size of the matrix elements at the fiber/matrix interface and at the model edge, where A-CNT forest starts, is $5R_{CNT}$. Other matrix elements that host CNTs have a size of $8R_{CNT}$, and further from CNTs, their size is $40R_{CNT}$, where R_{CNT} is the outer radius of a nanotube (9 nm). For nanotubes, 4-node general-purpose conventional shell elements were chosen with the outer surface of the nanotube used as the reference surface. The length of the nanotube mesh element along the nanotube varies from $1R_{CNT}$ to $20R_{CNT}$ depending on the curvature of the nanotube, and the width of the nanotube mesh element corresponds to 8 nodes at the circumference. The translational degrees of freedom of the nanotube nodes were constrained to the interpolated values of the corresponding degrees of freedom of the corresponding host elements, whereas the rotational degrees of freedom of the shell elements were not constrained by the embedding.

Horizontal and vertical displacements, measured by μDIC on the edges of the region of interest, were applied to the FE model (Fig. 4a) as boundary conditions. In the fiber direction, periodical boundary conditions were applied. *ABAQUS/Standard* (*Dassault*

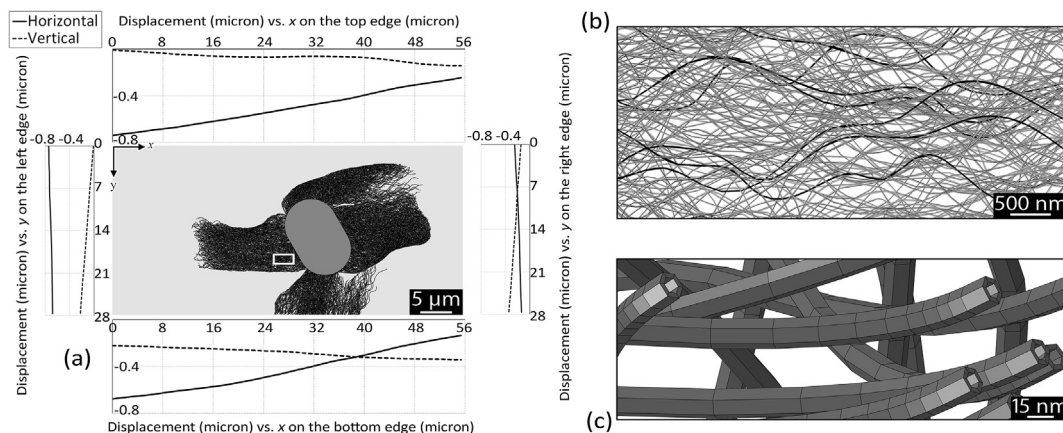


Fig. 4. (a) FE model of the selected region of interest from the study zone, simulating A-CNTs grown on the surface of *Fiber 1*, with the μDIC -measured displacements profiles on each edge of the region of interest; (b) zoom-in configuration of an A-CNT forest region, marked with the small white window in (a); (c) hollow CNTs in the model.

Systemes) and the associated pre-processor, ABAQUS/CAE, were used for numerical analysis.

5. Results and discussion

The results shown in this section correspond to the last (10th) step of deformation unless other steps are specified. For the ease of interpretation, the edges of the alumina fibers and A-CNT forests are marked respectively by solid and dashed lines, in three different colors, in all μ DIC resulting maps. The value of the parameter σ ("the 1-standard deviation confidence of the match", calculated in VIC-2D 2009), which can be used to estimate the image correlation uncertainty, is between 0.0041 and 0.0211 pixels, all over the study zone. This means that 99.7% of the resulting displacement values have a maximum deviation of 0.0633 ($3 \times \sigma_{max}$) pixels ($\pm 0.0046 \mu\text{m}$) from the expected value, which can differ from the real value due to physical errors. Therefore, the image correlation

uncertainty in the displacement analysis (corresponding to the measurement error explained in Section 3.3) is estimated to be below 5 nm. The significance of this uncertainty should be assessed when reporting the μ DIC results. It is worth noting that the maximum value for σ in all the previous deformation steps is less than 0.0211 pixels.

5.1. Displacement analysis

Horizontal (x -direction) and vertical (y -direction) displacement maps measured by μ DIC are presented in Fig. 5a and b. The rigid-body displacement of the study zone is largely compensated by locating the study zone in each deformation step before image acquisition. Still, the relative displacement between two points, and thus, the strain values are not affected by the rigid-body displacement. In Fig. 5a, the gradual change in the horizontal strain in the x direction and almost constant horizontal strain in the y direction

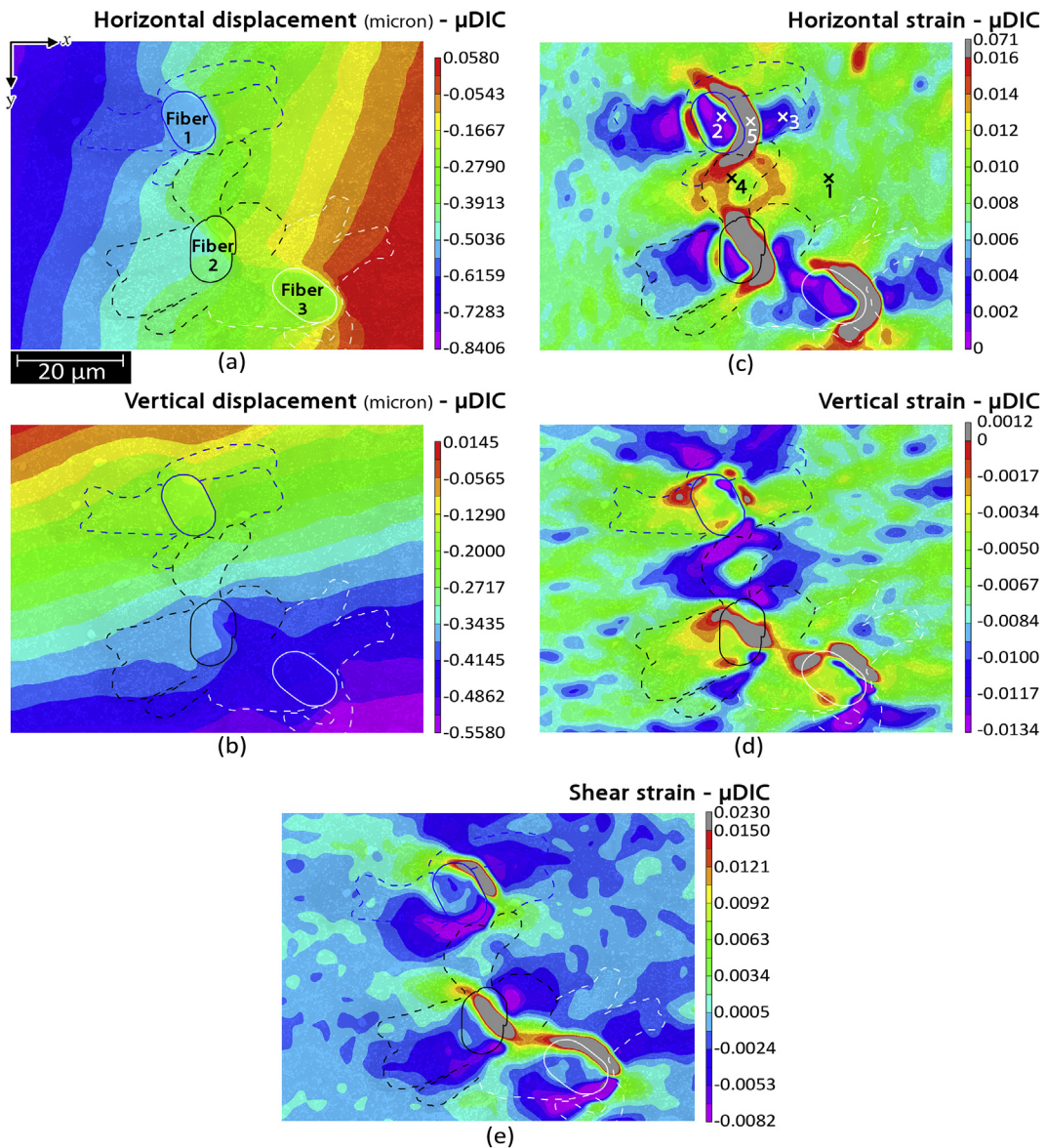


Fig. 5. (a) Horizontal and (b) vertical μ DIC resulting displacement maps, and (c) horizontal, (b) vertical, and (e) shear μ DIC resulting strain maps on the study zone, corresponding to the last (10th) step of deformation – the numbered crosses indicated on (c) are points on 1: matrix, 2: fiber, 3: horizontal A-CNT forest, 4: vertical A-CNT forest, and 5: debonded region, for local strain history analysis.

confirm that the study zone is horizontally loaded in the x direction. Fig. 5a also shows that the study zone is situated on the left side of the specimen since the absolute values of displacement increase when moving toward the negative x direction. The presence of the fibers distorts the displacement fronts due to their high stiffness. The A-CNT forests also influence the displacement fronts. This effect is further discussed in Section 5.2.

Fig. 5b shows similar results for the vertical displacement. Nearly horizontal displacement fronts confirm contraction in the y direction. The vertical displacement increases toward the bottom of the study zone and the fronts are again distorted by the fibers. Fig. 6 displays the horizontal and vertical displacement maps on the smaller region of interest including *Fiber 1*, resulted from FEA in comparison with the μ DIC results for the same region. The comparison of displacement plots in Fig. 6a, b, e and f indicates that μ DIC captures well the heterogeneity of the material through displacements. A more detailed comparison along different paths shows that the agreement is exceptional. In Fig. 6c, the model underpredicts the level of the horizontal displacement on the left side of the fiber. This is likely due to a more extended debonded region in the experiment that increases compliance of the material locally.

5.2. Strain analysis

The average horizontal and vertical strains, in the region of interest, resulted from μ DIC are 0.008939 (stretching) and -0.007207 (contraction), respectively. This shows higher deformation in the x direction than in the y direction. Furthermore, the average horizontal strain is close to the value of virtual strain (0.008462), applied in strain deviation analysis in Section 3 for parameter optimization and error analysis. Therefore, with the optimized parameters, similar level of measurement errors, estimated in Section 3, are expected. The average horizontal and vertical strains calculated through FEA are 0.009440 and -0.007746 , respectively. The μ DIC average strains are within 7% of the predicted ones.

Fig. 5c, d and e shows the horizontal, vertical, and shear strain maps obtained through DIC. High strains are observed around and on the fibers, revealing openings in fiber/matrix interface (debonding) or in fiber cross-section due to fiber fracture, respectively. In the presence of such high deformations, other micro-structural features with low deformation become invisible in the strain maps. To expose these features, the upper legend limit of the horizontal strain map is reduced to 0.015, and that of the vertical strain map to zero. The outlying strains, corresponding to the interfacial or fiber openings, are arbitrarily shown in gray. Debonding at the fiber/matrix interface typically undergoes three stages, as observed by X-ray microtomography in Ref. [36], (i) interfacial debond initiation at the free surface, (ii) progressive debonding at the free surface as well as along the fiber, and (iii) debond crack tunneling. In the present work, where the interface is initially debonded before loading, we are able to monitor a part of stage (ii) via 2D μ DIC.

Fig. 5c shows that the x -direction component of the interfacial and fiber openings is captured around fibers and on the fiber break (gray e.g. *Point 5*). The strain in the x direction is positive all over the matrix, representing tension (green/yellow e.g. *Point 1*). Due to the high stiffness of the fibers, they undergo much lower strains (purple/blue e.g. *Point 2*). A-CNT forests that are aligned in the x direction (horizontal A-CNT forests) are also easily identified in the strain maps. Because of the high stiffness, A-CNTs constrain tensile deformation in their longitudinal direction. This is reflected in low strains in that direction (purple/blue e.g. *Point 3*). The constraining effect would have been even more pronounced if the nanotubes were perfectly straight. Waviness of nanotubes, which is also

present here, is known to significantly reduce the nanocomposite stiffness [37]. The strain is not constrained by A-CNT forests that are (almost) perpendicular to the loading direction (vertical A-CNT forests) (red e.g. *Point 4*). This is well expected since the impregnated A-CNT forest behaves as a quasi-unidirectional nanocomposite, transverse properties of which are dominated by the matrix behavior.

The vertical strain map (Fig. 5d) represents negative strain all over the matrix (green), verifying that the study zone is under compression in the y direction. Fibers are detected by their low strain (light green/yellow). Higher vertical strains are captured at the fiber/matrix interface and the fiber break, due to the opening and shearing of the traction free regions. The presence of A-CNT forests aligned in the x direction is hardly detectable through the strain in the y direction. It is because their transverse behavior is controlled by the matrix. A-CNT forests that are not perfectly horizontal show constrained vertical strain due to CNTs' contribution into the matrix stiffness (light green/yellow). The shear strain map (Fig. 5e) likewise represents micro-features in the study zone.

For more quantitative analysis, μ DIC results are evaluated along two horizontal lines; one intersecting an alumina fiber (*Fiber 1*) with two horizontal A-CNT forests on the sides (path *a* in Figs. 6 and 7), and the other one intersecting vertical A-CNT forests (path *b* in Figs. 6 and 7). The length of path *a* and path *b* is 52.1 μm and 45.6 μm , respectively. Fig. 6c shows the horizontal displacement profile along path *a*. Based on the change in the displacement, the plot can be divided into 7 quasi-linear segments of 4 different features: matrix, fiber, A-CNT forest, and debonded region. With regard to the slope of the quasi-linear segments, representing an average horizontal strain along path *a* in that segment, the features are ordered as fiber, A-CNT forest, matrix, and the debonded region. This confirms that the A-CNTs aligned with the loading direction constrain the tensile deformation while the presence of the debonded region makes the material more compliant. Fig. 6d displays the horizontal displacement along path *b*. Because of the vertical alignment of the A-CNT forests, their effect on the horizontal displacement field is not detected. Similarly, the vertical displacements are extracted along both paths (Fig. 6g and h).

Fig. 7d shows the horizontal strain along path *a*. The two extremely high strain peaks correspond to the two debonded regions around *Fiber 1*. The fiber experiences a low strain that is constant over the fiber width and identifiable by a distinctive plateau. The strain is lower in the horizontal A-CNT forests than in the matrix, and gradually increases to the matrix strain value when moving from the fiber toward the matrix. Fig. 7e shows horizontal strains for the vertical A-CNT forests, along path *b*. The vertical strain profiles along both paths (Fig. 7i and j) follow a similar trend as the corresponding horizontal strain profiles do. The modeling results are also shown in Figs. 6 and 7. The trends of the plots are in general agreement with those of μ DIC, meaning that both methods could recognize features as small as several microns based on deformation. In particular, for path *b*, along which large deformation gradients do not occur, the agreement is better. The differences can be attributed to the μ DIC errors (mentioned in Section 3), averaging and smoothing in DIC, but also simulation assumptions. For instance, the discrepancy between μ DIC and FEA results for the horizontal displacement and strain on the left side of *Fiber 1*, along path *a* (Figs. 6c and 7d), is suspected to be due to the difference in modeling of the interface debonding from reality. In the experiment, the debonding progresses around and/or along the fiber, while the progression of the debonding is not taken into account in the modeling. This reasoning is supported by the fact that the difference between the μ DIC and FEA results is small under low load levels, and increases with the load increase, as observed in Fig. 8b.

To confirm that the heterogeneity in strain maps comes from the

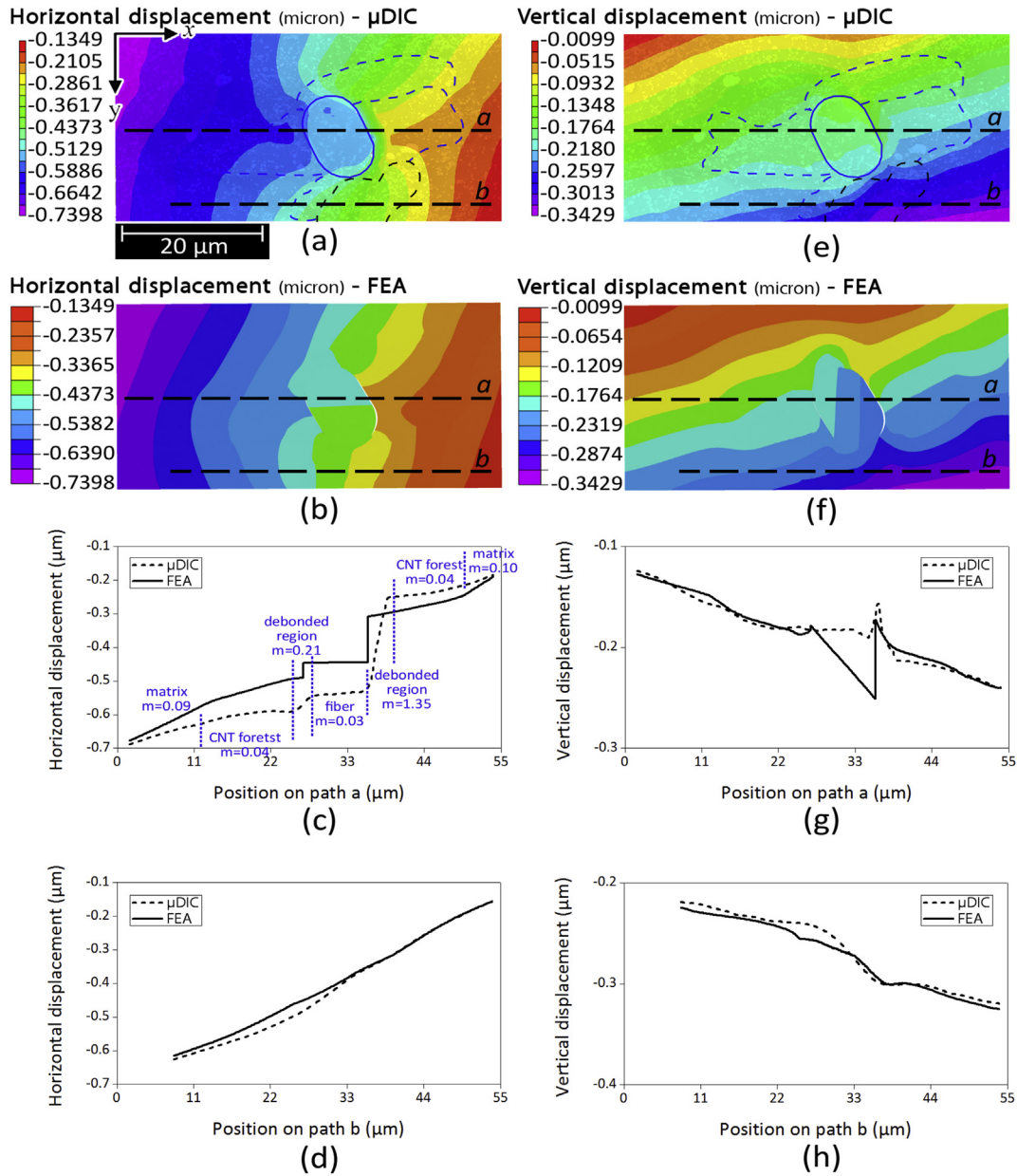


Fig. 6. Horizontal (a, b, c, d) and vertical (e, f, g, h) displacement maps on the small region of interest, and displacements along path *a* and *b* (shown on the corresponding displacement maps), measured by μ DIC and predicted by FEA, corresponding to the last (10th) step of deformation – features identified by DIC, based on their horizontal displacement are shown on (c) whereas *m* represents the slope of each quasi-linear segment.

presence of A-CNTs, the FE model is also run for the composite without the nano-reinforcement. The maps, which are shown in Fig. 7c and h, show strain concentrations near debonded regions, but no constrained deformation on both sides of the fiber, which proves that the strain heterogeneity is due to the nanotubes. Comparison of these strain maps with the predicted maps corresponding to the presence of A-CNTs (Fig. 7b and g) confirms that the strain heterogeneity is due to a high stiffness of A-CNTs in the alignment direction. This can be concluded also by comparison of the FEA-predicted strain profiles along path *a* and *b* for the model with and without the nano-reinforcement (Fig. 7d, e, i and j).

The local strain history of each analysis point can be used as a measure of reliability of μ DIC results for that point, in the elastic deformation cases [13]. The history of the μ DIC horizontal strain of five points on five different features (indicated with numbered

crosses in Fig. 5c) is plotted in Fig. 8a. For each feature, the local strain is plotted versus the μ DIC average strain of the study zone, in each deformation step. Assuming the loading stays in the elastic regime, the local strain histories are fitted firstly with a line, intercepting the origin. The first two steps are excluded since their corresponding micrographs were slightly out of focus. The resulting coefficient of determination (R^2) values for the points on the matrix, horizontal A-CNT forest, vertical A-CNT forest, debonded region, and fiber are 0.99, 0.97, 0.99, 0.93, and 0.04, respectively. This proves that the measurement results are accurate for the matrix and A-CNT forests. The lower R^2 for the debonded region, while it has high strain values, can be easily explained by the non-linear trend of its strain history. This non-linearity is in agreement with the trend observed in Ref. [36], where the debonded region propagated in function of the applied load.

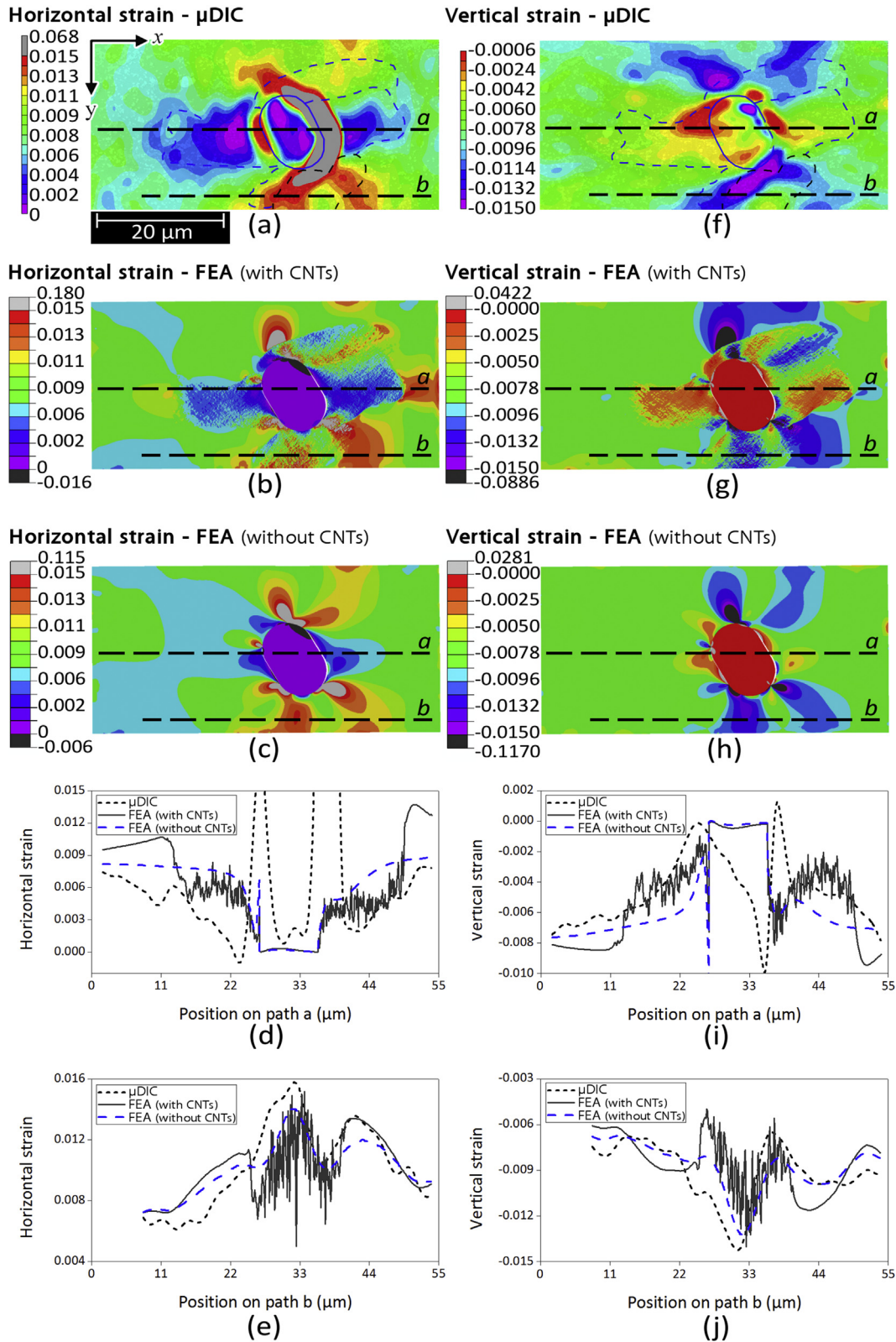


Fig. 7. Horizontal (a, b, c, d, e) and vertical (f, g, h, i, j) strain maps on the small region of interest, and strains along path *a* and *b* (shown on the corresponding strain maps), measured by μ DIC and predicted by FEA, corresponding to the last (10th) step of deformation for the model with and without the nano-reinforcement.

Opening of the existing debonding without its propagation would have resulted in a linear dependence. To confirm this, FEA was used to obtain this dependence for the debonded region, of

which the size was fixed during the deformation. In Fig. 8b, the normal opening of the debonded region on the right side of *Fiber 1*, measured through μ DIC, is plotted next to the FEA-calculated

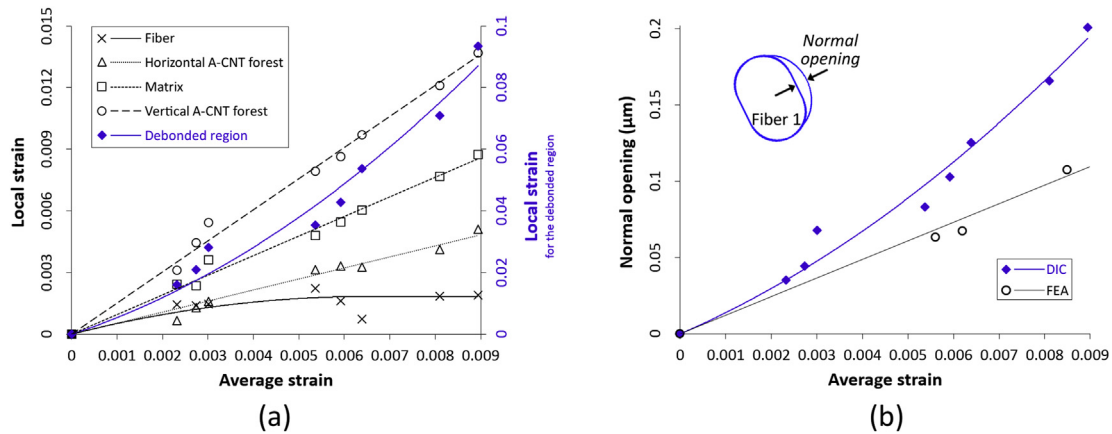


Fig. 8. (a) Horizontal local strains, obtained through DIC, in different locations (indicated in Fig. 5c by numbered crosses) with corresponding fitting curves and (b) normal opening of the right-side interface of *Fiber 1*, measured by μ DIC and calculated through FEA, versus the resulting average strain of the study zone in each deformation step – except for the debonded region, which is fitted with a quadratic, and the fiber, which has reached a plateau, the strain history of the other features is fitted with a linear function.

opening. The FEA-calculated opening increases linearly with the applied deformation. This means that the experimentally detected non-linearity in the opening of the debonding is due to the propagation of the debonding around, and/or along the fiber, and/or its kinking into the matrix. Without the presence of these additional mechanisms, the opening of the debonding would have been linear as predicted by the simulations. When corrected with a quadratic fitting, R^2 becomes 0.97 for the debonded region. The low linearity for the fiber ($R^2 = 0.04$), beside higher charging, less speckles, and smaller deformation of fibers, is likely due to the propagation of the debonded region, which reduces load transfer to the fiber. This is identified in Fig. 8a with a plateau for strain history of the fiber after average strain of ~ 0.004 . It is remarkable that μ DIC is capable of capturing surface openings as small as 35 nm for the debonded region (Fig. 8b), with the correlation uncertainty of ~ 5 nm.

6. Concluding remarks

The potential of micro-scale DIC to analyze deformation in fiber-reinforced composites with nano-scale modifications was evaluated for the first time. The high-quality random speckle pattern, produced by deposition of alumina nano-particles, together with optimized DIC parameters and proper microscopy settings provided displacement and strain maps with high-precision. Features such as fiber, matrix, A-CNT forest, and debonded regions at the fiber/matrix interface could be detected in both displacement and strain analyses. Openings as small as 35 nm in the debonded regions could be measured. The image correlation uncertainty in the displacement analysis was found to be below 5 nm, as estimated from the standard deviation confidence of the match. Furthermore, the μ DIC results were compared with predictions of a two-scale numerical model, and a good agreement between the two approaches was observed. As a side achievement, a non-linear trend in the opening of the debonded region in function of the applied deformation was observed indicating propagation of debonding around and/or along the fiber. The μ DIC was found to be a promising instrument in evaluation of the effects of nano-scale reinforcements on the deformation of hierarchical materials. Further progress in μ DIC is needed, particularly in the improvement of correlation methods to distinguish different phases, on which subset averaging is performed. This will allow even higher precisions in capturing deformation gradients at interfaces of materials with high mismatch in properties.

Acknowledgements

The authors would like to acknowledge support of Skolkovo Institute of Science and Technology through the No. 335-MRA project linked to the Center for Design, Manufacturing and Materials. The technical support of Tom Van der Donck in image acquisition is also highly appreciated.

References

- [1] M.A. Sutton, J.-J. Orteu, H. Schreier, *Image Correlation for Shape, Motion and Deformation Measurements: Basic Concepts, Theory and Applications*, Springer Publishing Company, 2009. Incorporated.
- [2] B. Pan, K. Qian, H. Xie, A. Asundi, Two-dimensional digital image correlation for in-plane displacement and strain measurement: a review, *Meas. Sci. Technol.* 20 (6) (2009).
- [3] S.V. Lomov, P. Boisse, E. Deluycker, F. Morestin, K. Vanclooster, D. Vandepitte, et al., Full-field strain measurements in textile deformability studies, *Compos. Part A Appl. Sci. Manuf.* 39 (8) (2008) 1232–1244.
- [4] A. Willems, S.V. Lomov, I. Verpoest, D. Vandepitte, Optical strain fields in shear and tensile testing of textile reinforcements, *Compos. Sci. Technol.* 68 (3–4) (2008) 807–819.
- [5] G. Catalanotti, P.P. Camanho, J. Xavier, C.G. Dávila, A.T. Marques, Measurement of resistance curves in the longitudinal failure of composites using digital image correlation, *Compos. Sci. Technol.* 70 (13) (2010) 1986–1993.
- [6] T. He, L. Liu, A. Makeev, B. Shonkwiler, Characterization of stress–strain behavior of composites using digital image correlation and finite element analysis, *Compos. Struct.* 140 (2016) 84–93.
- [7] A. Tatschl, O. Kolednik, A new tool for the experimental characterization of micro-plasticity, *Mater. Sci. Eng. A Struct. Mater. Prop. Microstruct. Process.* 339 (1–2) (2003) 265–280.
- [8] F. Lagattu, F. Bridier, P. Villechaise, J. Brillaud, In-plane strain measurements on a microscopic scale by coupling digital image correlation and an in situ SEM technique, *Mater. Charact.* 56 (1) (2006) 10–18.
- [9] M.A. Sutton, N. Li, D.C. Joy, A.P. Reynolds, X. Li, Scanning electron microscopy for quantitative small and large deformation measurements part i: SEM imaging at magnifications from 200 to 10,000, *Exp. Mech.* 47 (6) (2007) 775–787.
- [10] A.D. Kammers, S. Daly, Digital image correlation under scanning electron microscopy: methodology and validation, *Exp. Mech.* 53 (9) (2013) 1743–1761.
- [11] M.A. Sutton, N. Li, D. Garcia, N. Cornille, J.J. Orteu, S.R. McNeill, et al., Scanning electron microscopy for quantitative small and large deformation measurements part II: experimental validation for magnifications from 200 to 10,000, *Exp. Mech.* 47 (6) (2007) 789–804.
- [12] L.P. Canal, C. Gonzalez, J.M. Molina-Aldareguia, J. Segurado, J. Llorca, Application of digital image correlation at the microscale in fiber-reinforced composites, *Compos. Part A Appl. Sci. Manuf.* 43 (10) (2012) 1630–1638.
- [13] M. Mehdikhani, M. Aravand, B. Sabuncuoglu, M.G. Callens, S.V. Lomov, L. Gorbatikh, Full-field strain measurements at the micro-scale in fiber-reinforced composites using digital image correlation, *Compos. Struct.* 140 (2016) 192–201.
- [14] H. Qian, E.S. Greenhalgh, M.S.P. Shaffer, A. Bismarck, Carbon nanotube-based hierarchical composites: a review, *J. Mater. Chem.* 20 (23) (2010) 4751–4762.
- [15] A.S. Wu, T.-W. Chou, Carbon nanotube fibers for advanced composites, *Mater.*

- Today 15 (7–8) (2012) 302–310.
- [16] E.J. Siochi, J.S. Harrison, Structural nanocomposites for aerospace applications, *MRS Bull.* 40 (10) (2015) 829–835.
- [17] L. Gorbatikh, B.L. Wardle, S.V. Lomov, Hierarchical lightweight composite materials for structural applications, *MRS Bull.* 41 (9) (2016) 672–677.
- [18] G. Dai, L. Mishnaevsky, Fatigue of multiscale composites with secondary nanoplatelet reinforcement: 3D computational analysis, *Compos. Sci. Technol.* 91 (2014) 71–81.
- [19] L. Mishnaevsky, G. Dai, Hybrid and hierarchical nanoreinforced polymer composites: computational modelling of structure-properties relationships, *Compos. Struct.* 117 (2014) 156–168.
- [20] V.S. Romanov, S.V. Lomov, I. Verpoest, L. Gorbatikh, Modelling evidence of stress concentration mitigation at the micro-scale in polymer composites by the addition of carbon nanotubes, *Carbon* (2014) 1–11.
- [21] V.S. Romanov, S.V. Lomov, I. Verpoest, L. Gorbatikh, Can carbon nanotubes grown on fibers fundamentally change stress distribution in a composite? *Compos. Part A Appl. Sci. Manuf.* 63 (2014) 32–34.
- [22] V. Romanov, S.V. Lomov, I. Verpoest, L. Gorbatikh, Inter-fiber stresses in composites with carbon nanotube grafted and coated fibers, *Compos. Sci. Technol.* 114 (0) (2015) 79–86.
- [23] N. Yamamoto, A. John Hart, E.J. Garcia, S.S. Wicks, H.M. Duong, A.H. Slocum, et al., High-yield growth and morphology control of aligned carbon nanotubes on ceramic fibers for multifunctional enhancement of structural composites, *Carbon* 47 (3) (2009) 551–560.
- [24] M.A. Aravand, O. Shishkina, I. Straumit, A.H. Liotta, S.S. Wicks, B.L. Wardle, et al., Internal geometry of woven composite laminates with “fuzzy” carbon nanotube grafted fibers, *Compos. Part A Appl. Sci. Manuf.* 88 (2016) 295–304.
- [25] E.J. Garcia, B.L. Wardle, A. John Hart, N. Yamamoto, Fabrication and multifunctional properties of a hybrid laminate with aligned carbon nanotubes grown in situ, *Compos. Sci. Technol.* 68 (9) (2008) 2034–2041.
- [26] J.-P. Salvetat-Delmotte, A. Rubio, Mechanical properties of carbon nanotubes: a fiber digest for beginners, *Carbon* 40 (10) (2002) 1729–1734.
- [27] E.J. Garcia, A.J. Hart, B.L. Wardle, Long carbon nanotubes grown on the surface of fibers for hybrid composites, *AIAA J.* 46 (6) (2008) 1405–1412.
- [28] P. Auerkari, Mechanical and Physical Properties of Engineering Alumina Ceramics, Technical Research Centre of Finland, 1996.
- [29] S. Xie, W. Li, Z. Pan, B. Chang, L. Sun, Mechanical and physical properties on carbon nanotube, *J. Phys. Chem. Solids* 61 (7) (2000) 1153–1158.
- [30] Y.A. Kim, T. Hayashi, M. Endo, Y. Kaburagi, T. Tsukada, J. Shan, et al., Synthesis and structural characterization of thin multi-walled carbon nanotubes with a partially faceted cross section by a floating reactant method, *Carbon* 43 (11) (2005) 2243–2250.
- [31] V.M.C.F. Cunha, J.A.O. Barros, J.M. Sena-Cruz, A finite element model with discrete embedded elements for fibre reinforced composites, *Comput. Struct.* 94–95 (2012) 22–33.
- [32] V.S. Romanov, S.V. Lomov, I. Verpoest, L. Gorbatikh, Stress magnification due to carbon nanotube agglomeration in composites, *Compos. Struct.* 133 (2015) 246–256.
- [33] A. Matveeva, H.J. Bohm, G. Kravchenko, F.W.J. van Hattum, Investigation of the embedded element technique for modelling wavy CNT composites, *Comput. Mater. Continua* 42 (1) (2014) 1–23.
- [34] A. Matveeva, V. Romanov, S. Lomov, L. Gorbatikh, Application of the Embedded Element Technique to the Modelling of Nano-Engineered Fiber-Reinforced Composites, 2015.
- [35] V.S. Romanov, Modelling Tools for Micro-Scale Stress Analysis of Nano-Engineered Fibre-Reinforced Composites, University of Leuven, 2015.
- [36] K. Martyniuk, B.F. Sorensen, P. Modregger, E.M. Lauridsen, 3D in situ observations of glass fibre/matrix interfacial debonding, *Compos. Part A Appl. Sci. Manuf.* 55 (2013) 63–73.
- [37] I.Y. Stein, D.J. Lewis, B.L. Wardle, Aligned carbon nanotube array stiffness from stochastic three-dimensional morphology, *Nanoscale* 7 (46) (2015) 19426–19431.